Detectability of a phase transition in neutron star matter with third-generation gravitational wave interferometers

C Mondal, M Antonelli, F Gulminelli, M Mancini, J Novak, M Oertel

Monthly Notices of the ROYAL ASTRONOMICAL SOCIETY

MNRAS **524,** 3464–3473 (2023) https://doi.org/10.1093/mnras/stad2082
Advance Access publication 2023 July 11

Detectability of a phase transition in neutron star matter with third-generation gravitational wave interferometers

C. Mondal [1,2★] M. Antonelli,[1] F. Gulminelli [1★] M. Mancini,[3,4] J. Novak[4] and M. Oertel[4★]

[1]*Laboratoire de Physique Corpusculaire, CNRS, ENSICAEN, UMR6534, Université de Caen Normandie, F-14000, Caen Cedex, France*
[2]*Institut d'Astronomie et d'Astrophysique, Université Libre de Bruxelles, CP 226, B-1050 Brussels, Belgium*
[3]*IDP, UMR 7013, CNRS, University Orléans, University Tours, Université d'Orléans, rue de Chartres, BP 6759, F-45067 Orléans Cedex 2, France*
[4]*Laboratoire Univers et Théories, Observatoire de Paris, Université PSL, CNRS, F-92190 Meudon, France*

Accepted 2023 July 7. Received 2023 July 5; in original form 2023 May 25

ABSTRACT

Possible strong first-order hadron-quark phase transitions in neutron star interiors leave an imprint on gravitational waves, which could be detected with planned third-generation interferometers. Given a signal from the late inspiral of a binary neutron star (BNS) coalescence, assessing the presence of such a phase transition depends on the precision that can be attained in the determination of the tidal deformability parameter, as well as on the model used to describe the hybrid star equation of state. For the latter, we employ here a phenomenological meta-modelling of the equation of state that largely spans the parameter space associated with both the low-density phase and the quark high density compatible with current constraints. We show that with a network of third-generation detectors, a single loud BNS event might be sufficient to infer the presence of a phase transition at low baryon densities with an average Bayes factor $B \approx 100$, up to a luminosity distance ($\mathcal{D}_{\rm L} \lesssim 300$ Mpc).

Key words: gravitational waves – instrumentation: interferometers – stars: neutron – neutron star mergers.

1 INTRODUCTION

In the standard picture, the interior of a neutron star (NS) encompasses several phases of matter, from nuclei in the iron region close to the surface via more exotic neutron-rich nuclear clusters in the crust to a uniform liquid of nuclear matter in the outer core (Haensel, Potekhin & Yakovlev 2007). In the core, at densities above nuclear saturation, $n_0 \approx 0.16\,\mathrm{fm}^{-3}$, the pressure becomes so high that further degrees of freedom may emerge. These include, possibly, mesons – which could also form condensates, hyperons or Δ-baryons. An even more dramatic possibility is that of a phase transition (PT) to degenerate quark matter and the formation of so-called hybrid stars. Under the hypothesis of absolutely stable strange quark matter, even pure quark stars might exist, see e.g. the reviews (Chamel & Haensel 2008; Oertel et al. 2017; Burgio & Fantina 2018; Lattimer 2019; Raduta 2022). This makes the compact objects a unique testbed of subatomic physics, not only probing nuclear many-body phenomena and their dependence on density and isospin asymmetry, i.e. the neutron-to-proton ratio but also probing unexplored finite-density regimes of quantum chromodynamics.

Currently, the main astrophysical constraints on NS interiors stem from the precise mass determinations for three NSs in NS-white dwarf systems (Demorest et al. 2010; Antoniadis et al. 2013; Fonseca et al. 2016; Cromartie et al. 2019), all three with gravitational masses around 2 $M_\odot$. The object PSR J0740+6620 (Cromartie et al. 2019) is thereby particularly interesting since NICER succeeded in obtaining a measurement of its radius (Miller et al. 2021; Riley et al. 2021), making it the second object after PSR J0030+0451 (Miller et al. 2019; Riley et al. 2019) for which both mass and radius could be determined. Moreover, with the detections of gravitational waves (GW) from binary neutron star (BNS) mergers by the LIGO-Virgo collaboration, a new window has opened to explore the constituents of matter under extreme conditions. For the first detected event, GW170817, the tidal deformability was obtained (Abbott et al. 2017), a quantity strongly correlated with the NS radius. In the coming years, starting with run O4 of the LIGO-Virgo-Kagra (LVK) collaboration, GW detector network sensitivity will be further increased and a number of additional detections is expected. Projects for ground-based third-generation detectors such as the European einstein telescope (ET; Punturo et al. 2010; Maggiore et al. 2020) and the American cosmic explorer (CE; Reitze et al. 2019; Evans et al. 2021) planned for ∼2035 will allow for a considerable gain in sensitivity. They need more stringent constraints on theoretical models for the description of the dense matter.

A particular question in this context is the possible presence of a first-order PT in dense NS matter. Since the first mention of possible hybrid stars decades ago, e.g. (Glendenning, Weber & Moszkowski 1992), finding astrophysical signatures of such a PT has been a very active field of research, see for instance the reviews (Alford 2001; Buballa et al. 2014; Contrera et al. 2022). In this work, we investigate if and how accurately we can detect a PT in the core of two coalescing NSs during the inspiral phase with a network of third-generation GW detectors. Several authors have already pointed out that a PT in the post-merger phase leads to a characteristic increase in the dominant post-merger oscillation frequency (Bauswein et al. 2019; Most et al. 2019) with respect to the one expected from the measured inspiral parameters under the assumption of a purely baryonic equation of state (EoS). If the post-merger signal is detected it could even help to constrain the onset density for the PT (Blacker et al. 2020) and a delayed PT could leave an imprint on the ringdown of the black hole

★ E-mail: chiru.rkm@gmail.com (CM); gulminelli@lpccaen.in2p3.fr (FG); micaela.oertel@obspm.fr (MO)

formed once the metastable remnant has collapsed (Weih, Hanauske & Rezzolla 2020). These ideas apply if, prior to the merger, both stars do not present any PT, which is plausible for not too massive stars.

The horizon for detecting a post-merger signal is, however, relatively small even for third-generation detectors and only a few events are expected, see e.g. (Torres-Rivas et al. 2019). On the contrary, a huge number of BNS mergers should be detected with information extracted from the inspiral among others about the chirp mass $\mathcal{M}_c$, the mass ratio q and on the combined tidal deformability $\tilde{\Lambda}$ (see equation 15), which is a function of the tidal deformabilities Λ_1 and Λ_2 of both stars (Maggiore et al. 2020; Evans et al. 2021; Branchesi et al. 2023). Since a PT changes the relation between the mass and the tidal deformability for each star, (see e.g. Damour & Nagar 2009; Postnikov, Prakash & Lattimer 2010; Han & Steiner 2019; Sieniawska et al. 2019), $\tilde{\Lambda}$ is modified, and this of course raises the question of its detectability which many studies have addressed recently.

For instance, based on the breakdown of quasi-universal relations fitted to purely hadronic EoS in (Chatziioannou & Han 2020) and a comparison of the inferred radius in (Chen, Chesler & Loeb 2020) together with a collection of simulated BNS merger events for purely hadronic and hybrid EoS, it has been shown that ∼50–100 detections can be sufficient to distinguish different EoSs. In Coupechoux et al. (2023), the authors assess the possibility to distinguish different equations of state with and without a PT from a GW170817-like event during the O4 run of LVK. The importance of next-generation detectors (ET and CE) to identify a hadron-quark PT was pointed out by some recent studies based on e.g. different behaviour of the sound speed (Tan et al. 2022), or breaking the degeneracy of EoS models with similar NS radii but different tidal deformabilities (Raithel & Most 2023). The above studies, however, conclude on the detectability of a PT by comparing a few particular EoS models, which is clearly not sufficient to cover the entire space of all possible EoSs with and without PT. A different approach has been used in Essick et al. (2020) and Landry, Essick & Chatziioannou (2020), where a non-parametric EoS inference is applied to the GW170817 event with weak statistical evidence in favour of two stable branches, i.e. the existence of hybrid stars with a strong PT. The role of third-generation interferometers in reaching a more robust conclusion on this issue was pointed out in Landry & Chakravarti (2022). In the study by Pang et al. (2020), the authors have performed a Bayesian inference study with three different injected EoS models, concluding that already 12 events with current detectors could be sufficient to disentangle a strong PT. However, here the injected models represent only snapshots of all possible EoSs with a PT transition and the inference of a PT is done based on the number of different polytropes employed in the EoS reconstruction. We will use a meta-modelling approach as well for the models with PT as those without. The metamodel is a flexible parametrization of the purely nuclear EoS, incorporating constraints from nuclear experiments, theory, and astrophysical observations as priors (Margueron, Hoffmann Casali & Gulminelli 2018). For the former, we have extended the nuclear meta-model to include a potential PT taking as parameters the density for the onset of the transition, the energy density jump and the sound speed in the high-density phase controlling the stiffness of the EoS. The injection models have been chosen from the borders of the respective metamodels. In addition, we will concentrate here on the possibility to detect a PT from one single loud event in third-generation detectors.

The paper is organized as follows: In Section 2 we summarize the EoS modelling which is used in the present work. A brief summary of the Fisher matrix formalism to quantify variances in various astrophysical parameters connected to a BNS merger is provided in Section 4.2. Section 4 contains the proposed Bayesian framework to infer the possible signs of a PT from the GW gravitational wave signal generated by a BNS coalescence. We discuss the results in Section 5. Concluding remarks and the future extensions of the present work are discussed in Section 6.

2 METAMODELLING OF NEUTRON STAR MATTER

For our purposes, NS matter comprises an inhomogeneous crust and a core of uniform matter fully governed by the strong interaction. The crust and the purely nucleonic outer core are consistently calculated using the same energy functional, see Section 2.2. We describe then the core, see Section 2.1 in the nucleonic hypothesis up to a certain density, beyond which we assume the appearance of quarks at the very centre of the star. The density of the PT to the quark core is an input parameter in our model.

2.1 Neutron star core

2.1.1 Nucleonic part

For the description of the purely nucleonic outer core, we follow a metamodelling approach. Below we will briefly recall the main lines of the model, for details see Margueron et al. (2018). Within our model, the uniform nucleonic matter is described by decomposing the energy density of infinite nuclear matter as

$$\varepsilon_N(n_\mathrm{n}, n_\mathrm{p}) = C_\mathrm{kin} \sum_{q=n,p} \frac{n_q^{5/3}}{m_q^\star(n,\delta)} + U_0(n) + U_\mathrm{sym}(n)\,\delta^2\,, \tag{1}$$

where n_n (n_p) is the neutron (proton) number density, $n = n_\mathrm{n} + n_\mathrm{p}$ is the baryon number density, $\delta = (n_\mathrm{n} - n_\mathrm{p})/n$ is the isospin asymmetry and $C_\mathrm{kin} = 3(3\pi^2\hbar^3)^{2/3}/10 \approx 2.87\,\hbar^2$. The first term takes into account the zero point Fermi gas contribution, and the momentum dependence of the nuclear interaction through the density-dependent effective mass $m_q^\star\,(q = n, p)$. The remaining term is broken down into an isospin symmetric part, $U_0(n)$, and an isospin asymmetric part, $\delta^2\,U_{sym}(n)$. For both $U_0(n)$ and $U_\mathrm{sym}(n)$ an expansion up to order $N = 4$ around the nuclear saturation density n_sat is used:

$$U_{0,\mathrm{sym}}(n) = n \sum_{k=0}^{N} \frac{(v_k)_{0,\mathrm{sym}}}{k!}\, u_k^N(x)\, x^k\,, \tag{2}$$

with

$$x = \frac{n - n_\mathrm{sat}}{3n_\mathrm{sat}}, \quad \text{and,} \quad u_k^N(x) = 1 - (-3x)^{N+1-k}\,\mathrm{e}^{-b(1+3x)}, \tag{3}$$

where the u_k^N terms ensure vanishing energy at zero density. The coefficients $(v_k)_{0,\mathrm{sym}}$ are functions of nuclear matter properties (NMPs) at saturation density n_sat. Specifically, the coefficients of U_0 in equation (2) can be expressed as a function of the density derivatives at different orders of the energy per baryon of symmetric nuclear matter[1] (SNM), like the energy per particle E_sat, incompressibility K_sat, skewness Q_sat and kurtosis Z_sat. Similarly, the coefficients of U_sym are related to other NMPs, like the symmetry energy E_sym, symmetry slope L_sym, symmetry incompressibility K_sym, symmetry skewness Q_sym and symmetry kurtosis Z_sym, all evaluated at n_sat and for symmetric matter.

[1]Nuclear matter with an equal number of protons and neutrons, i.e. $\delta = 0$.

The contribution of an ideal gas of electrons (e) and muons (μ) to the energy density

$$\varepsilon_{e,\mu} = \frac{(m_{e,\mu})^4}{8\pi^2(\hbar c)^3}\left[(2x_r^2+1)x_r\gamma_r - ln(x_r+\gamma_r)\right], \quad (4)$$

where, $x_r = \frac{\hbar c(3\pi^2 n_l)^{1/3}}{m_l}$ and $\gamma_r = \sqrt{1+x_r^2}$ with $l = e, \mu$. The net amount of electrons present in the system is determined by the β-equilibrium condition solving the coupled equations of chemical potentials $\mu_{\rm n,p,e}$ of neutrons, protons and electrons, respectively, as

$$\mu_{\rm n}(n,\delta) - \mu_{\rm p}(n,\delta) = \mu_{\rm e}(n,\delta), \quad (5)$$

where $\mu_{\rm n,p} = \partial\varepsilon_N/\partial n_{\rm n,p} + m_{\rm n,p}c^2$, and $m_{\rm n,p}$ are the bare neutron and proton masses. If the chemical potential of electrons $\mu_{\rm e} = \partial\varepsilon_{\rm e}/\partial n_{\rm e}$ exceeds the muon mass m_μ, they appear spontaneously in NS matter. Their amount is fixed by local charge equilibrium $n_\mu = n_{\rm p} - n_{\rm e}$, and the global equilibrium condition $\mu_\mu = \mu_{\rm e}$. Once the equilibrium composition $\delta(n)$ is determined at each density from equation (5), the baryonic pressure is obtained from the thermodynamic relation[2]

$$p_N(n) = \sum_{q=n,p} n_q\left(\mu_q - m_q c^2\right) - \varepsilon_N(n,\delta). \quad (6)$$

where n_q, μ_q, and δ are all functions of n, while m_q are the two bare masses of neutrons and protons.

2.1.2 *Quark matter EoS*

We assume that the appearance of quarks in the inner core gives rise to a first-order PT, namely two continuous branches $p_N(\varepsilon_N)$, $p_Q(\varepsilon_Q)$ separated by a finite jump $\Delta\varepsilon$ in energy density at a given value $p_{\rm t}$ of the baryonic pressure. We note that $\varepsilon_{\rm t}$ is the highest value of the energy density in the nucleonic (N) phase, and $\varepsilon_t + \Delta\varepsilon$ represents the lowest energy density value in the quark phase. As a consequence, a discontinuity in the sound speed $c_{\rm s}$ between the nucleonic and quark phases is also expected. When the core gets converted to quarks completely, we assume it fixes $c_{\rm s}$ all the way up to the centre of the NS from the point of transition. In this simple picture, the EoS of the quark core can be specified by (see e.g. Zdunik & Haensel 2013; Alford & Sedrakian 2017):

$$p_Q(\varepsilon_Q) = c_{\rm s}^2(\varepsilon_Q - \varepsilon_{\rm t}), \quad (7)$$

$$\mu_Q(p_Q) = \mu_t\left[1 + \frac{1+c_{\rm s}^2}{c_{\rm s}^2}\frac{p_Q}{\varepsilon_{\rm t}}\right]^{c_{\rm s}^2/(1+c_{\rm s}^2)}, \quad (8)$$

$$n_Q(p_Q) = n_t\left[1 + \frac{1+c_{\rm s}^2}{c_{\rm s}^2}\frac{p_Q}{\varepsilon_{\rm t}}\right]^{1/(1+c_{\rm s}^2)} = n_{\rm t}\left(\frac{\mu_Q}{\mu_{\rm t}}\right)^{1/c_{\rm s}^2}. \quad (9)$$

Here, $\mu_{\rm t}$ represents the baryonic chemical potential at the transition point ($\mu_{\rm B} = \mu_{\rm n}$ in the nucleonic phase), and $n_{\rm t}$ is the baryonic density at the onset of the transition. Three parameters n_t, c_s^2, and $\Delta\varepsilon$ are used on top of the parameters for the nucleonic metamodelling to describe the NS core. In Zhang & Li (2023) a similar approach is used to model the NS EoS in order to obtain constraints on a potential hadron-quark transition from NS observables, but the nucleonic part in their case is limited to one single EoS, obtained by fixing the NMPs to a fiducial set.

[2]Note that according to equation (1), the metamodel energy density $\varepsilon_{\rm N}$ does not contain the mass terms, so they are explicitly added in equation (6).

2.2 Neutron star Crust

We model the NS crust by using the compressible liquid drop model (CLDM) approximation of Carreau, Gulminelli & Margueron (2019), which allows us to extend the metamodel for uniform nucleonic matter in Section 2.1.1. In the CLDM, the bulk energy of a spherical nucleus with A nucleons, Z protons, radius $r_{\rm N}$, and bulk density n_i is described by using equation (1) as $E_{\rm bulk} = A\varepsilon_N(n_i, 1-2Z/A)/n_i$. The total binding energy of a finite nucleus is obtained by adding surface, curvature, and Coulomb terms. The surface and curvature contributions are expressed in terms of surface and curvature tensions $\sigma_{\rm s}$ and $\sigma_{\rm c}$ as (Ravenhall, Pethick & Lattimer 1983; Maruyama et al. 2005; Newton, Gearheart & Li 2013)

$$E_{\rm surf} + E_{\rm curv} = 4\pi r_{\rm N}^2\left(\sigma_{\rm s}(Z/A) + \frac{2\sigma_{\rm c}(Z/A)}{r_{\rm N}}\right), \quad (10)$$

$$\text{with,} \quad \sigma_{\rm s}(x) = \sigma_0\frac{2^4 + b_{\rm s}}{x^{-3} + b_{\rm s} + (1-x)^{-3}}, \quad (11)$$

$$\sigma_{\rm c}(x) = 5.5\sigma_{\rm s}(x)\frac{\sigma_{0,\rm c}}{\sigma_0}(\beta - x). \quad (12)$$

Finally, the Coulomb term in a spherical Wigner–Seitz (WS) cell reads:

$$E_{\rm coul} = \frac{8}{3}\left(\pi {\rm e}\frac{Z}{A}n_i\right)^2 r_{\rm N}^5\,\eta_{\rm coul}\left(\frac{r_{\rm N}}{r_{\rm WS}}\right), \quad (13)$$

$$\text{with} \quad \eta_{\rm coul}(x) = \frac{1}{5}\left[x^3 + 2\left(1 - \frac{3}{2}x\right)\right]. \quad (14)$$

Here, e is the elementary charge, $r_{\rm WS}$ the radius of a WS cell, and $\eta_{\rm coul}$ the function taking into account electron screening in the Coulomb energy. The parameters $\sigma_0, \sigma_{0,c}, b_{\rm s}$, and β are obtained by optimizing the agreement of nuclear masses in vacuum with the AME2016 mass table (Wang et al. 2017; Dinh Thi, Fantina & Gulminelli 2021b; Dinh Thi et al. 2021c). The EoS is eventually obtained by minimizing the energy of the WS cell by varying A, Z, n_i, $r_{\rm N}$, $r_{\rm WS}$, as well as the neutron gas density $n_{\rm g}$ (Carreau et al. 2019; Dinh Thi et al. 2021b; Dinh Thi et al. 2021c).

3 ESTIMATION OF DETECTORS' RESPONSE: FISHER INFORMATION FORMALISM

In order to assess the uncertainty in the parameter estimation associated with future observations of GWs from the coalescence of BNSs, we make use of the publicly available tool GWBENCH (Borhanian 2021), which implements the Fisher information paradigm (Cutler & Flanagan 1994; Poisson & Will 1995). The main drawback of this approach is that it is valid for events with a high signal-to-noise ratio (SNR; Vallisneri 2008). On the other hand, its main advantage is the considerable increase in computational speed, as compared to standard Bayesian analysis. Here, we give a summary of our procedure to compute a sequence of simulated GW events from BNSs and estimate the parameters that could be inferred from such events by the third-generation Earth-based GW detectors. For details about GWBENCH, the interested reader can refer to Borhanian (2021).

We model events of BNS coalescence with masses m_1 and m_2 by using the waveform templates implemented in GWBENCH, namely the 'TaylorF2 + tidal' models (Wade et al. 2014). They depend on the following parameters: $\left(\mathcal{M}_c, \eta, \vec{\chi}_1, \vec{\chi}_2, \mathcal{D}_L, \iota, \tilde{\Lambda}, \delta\tilde{\Lambda}\right)$. Here, $\eta = m_1m_2/(m_1+m_2)^2$, $\vec{\chi}_{1,2}$ are the dimensionless spin vectors of the two NSs, $\mathcal{D}_{\rm L}$ is the luminosity distance, ι is the inclination angle of its orbital plane with respect to the line of sight. Finally, $\tilde{\Lambda}$ and $\delta\tilde{\Lambda}$ are two parameters containing the tidal deformabilities of both stars

(Λ_1, Λ_2) and are defined as:

$$\tilde{\Lambda} = \frac{8}{13}\left[\left(1+7\eta-31\eta^2\right)(\Lambda_1+\Lambda_2)+ \right. \\ \left. + \sqrt{1-4\eta}\left(1+9\eta-11\eta^2\right)(\Lambda_1-\Lambda_2)\right], \quad (15)$$

$$\delta\tilde{\Lambda} = \frac{1}{2}\left[\sqrt{1-4\eta}\left(1-\frac{13272}{1319}\eta+\frac{8944}{1319}\eta^2\right)(\Lambda_1+\Lambda_2)+ \right. \\ \left. + \left(1-\frac{15910}{1319}\eta+\frac{32850}{1319}\eta^2+\frac{3380}{1319}\eta^3\right)(\Lambda_1-\Lambda_2)\right]. \quad (16)$$

We use different EoS models as described in Section 2 to relate each NS mass (m_1, m_2) to the corresponding tidal deformability parameter (Λ_1, Λ_2). The M–Λ relation is obtained for each EoS by solving the Tolman–Oppenheimer–Volkov (TOV) equations, together with the differential equations for perturbed relativistic stars described by (Hinderer 2008, 2009). In the case where a PT appears in the NS, additional terms due to jumps in thermodynamic quantities must be taken into account. To do this, we follow the approach by Pereira et al. (2020).

For each EoS, we assume fixed values for the spins and inclination $\chi_1 = 0.01$, $\chi_2 = 0.005$, and $\iota = 45^\circ$ and inject a series of events into GWBENCH[3], with chosen values for the chirp mass $\mathcal{M}_c$, the mass ratio $q = m_2/m_1$ and the luminosity distance $\mathcal{D}_L$. $\tilde{\Lambda}$, and $\delta\tilde{\Lambda}$ are deduced from the M–Λ relation for the specific EoS considered and equations (15) and (16). The detector features are those of the projected third-generation ground-based ones: triangle-shaped ET (see Punturo et al. 2010) and two CE detectors (see Reitze et al. 2019). Details about their power spectral densities and exact projected locations are given in appendix C of Borhanian (2021). GWBENCH then returns estimates of measurement errors in the parameters of our waveform models. These estimates shall be used in the next sections, in particular for the case of $\tilde{\Lambda}$. Concerning $\delta\tilde{\Lambda}$, this parameter only enters at the sixth post-Newtonian (6 PN) order in the waveform, meaning, it is subdominant with respect to the leading-order 5 PN tidal correction (Wade et al. 2014). For this reason, it is not possible to obtain error-bound estimates of $\delta\tilde{\Lambda}$ within our approach; it can be however estimated using EoS-independent relations (Chatziioannou, Haster & Zimmerman 2018).

4 BAYESIAN FRAMEWORK

We use a Bayesian framework to quantify the compatibility of a simulated observation between a purely nucleonic and a hybrid (nucleons + quarks) NS core. For the different EoS, we employed the techniques outlined in Sections 2.1.1 and 2.2 based on Dinh Thi, Mondal & Gulminelli (2021a) and Mondal & Gulminelli (2023). To build the prior for the nucleonic metamodel, 12 NMPs corresponding to uniform matter[4] were varied randomly with a constant probability distribution over a wide domain. Since the expansion in equation (2) is truncated at the fourth order, it is necessary to use different $Q_{(\mathrm{sat,sym})}$ and $Z_{(\mathrm{sat,sym})}$ below and above n_{sat} to increase the reliability of the expansion over a large density range. In particular, it makes the EoS free of any fictitious correlations between observables connected more to the low and high-density regimes, respectively. Since these high-order NMPs have no contribution in equation (1) at n_{sat}, this way of choosing different values for coefficients of the same order in the expansion does not induce any discontinuity in the energy, pressure, or sound speed. This leads to a total of 16 parameters for the nucleonic EoS.

For the hybrid EoSs, containing nucleons and quarks, we obtained three families namely 'PT03', 'PT04', and 'PT05' based on the density n_t at the onset of the nucleon-quark transition fixed to 0.3, 0.4, and 0.5 fm^{-3}, respectively. For all hybrid models, the width of the plateau $\Delta\varepsilon$ is chosen by imposing a random value for the lowest baryon density in the quark phase varying between n_t and $1.5n_t$. Finally, the squared sound speed c_s^2 is randomly varied between 0.1 and 0.9 c^2, where c is the speed of light. These large variations were used to cover a large space in the $p(\varepsilon)$ plane by our hybrid models. It should be kept in mind, that a constant sound speed description can of course not recover a more complicated behaviour inherent to more sophisticated microscopic models for quark matter (see e.g. Kurkela, Romatschke & Vuorinen 2010; Chen et al. 2015; Xu et al. 2015; Zacchi, Hanauske & Schaffner-Bielich 2016; Alvarez-Castillo et al. 2019; Otto, Oertel & Schaefer 2020; Jokela et al. 2021; Shahrbaf et al. 2023), but the chosen range should be able to enclose most models such that we consider our assumptions as very conservative. It is quite important to mention here the particular motivation to keep n_t fixed at distinct values, rather than varying it randomly within a range, too. Since a random n_t would only introduce further uncertainty on top of the nucleonic EoS, the fully nucleonic metamodel would be systematically preferred irrespective of any observation. We thus target to identify the signature of nucleon-quark PT, based on its early or late appearance in terms of density.

4.1 Obtaining an informed prior

On the whole, to perform the Bayesian analysis we have used 16 parameters ($N_p = 16$) for the nucleonic metamodel and 19 parameters ($N_p = 19$) for 'PT03', 'PT04', and 'PT05' hybrid metamodels. The uninformed prior distribution $P_{\mathrm{prior}}(\mathbf{X}) = \prod_{k=1}^{N_p} P_k(X_k)$ of the parameter set $\mathbf{X} \equiv \{X_k,\ k = 1, \ldots N_p\}$ is obtained with a flat uncorrelated distribution $P_k(X_k)$. To obtain a prior informed by different observations, the probability of each model is then conditioned by the likelihood models of the AME2016 mass evaluation (Wang et al. 2017), low-density constraints on SNM and PNM obtained from theoretical χ-EFT calculations (Drischler, Hebeler & Schwenk 2016), constraint from the observed maximum mass of NS (Demorest et al. 2010; Antoniadis et al. 2013) and constraints on the joint tidal deformability $\tilde{\Lambda}$ of the GW170817 event (Abbott et al. 2019) as

$$P_{\mathrm{prior}}^{\mathrm{informed}}(\mathbf{X}) = P(\mathbf{X}|\mathbf{c}) = \mathcal{N}\cdot P_{AME2016}(\mathbf{X})P_{\chi-EFT}(\mathbf{X}) \\ \times P_{M_{\max}}(\mathbf{X})P_{GW170817}(\mathbf{X})\prod_k P(c_k|\mathbf{X}). \quad (17)$$

Here, $\mathcal{N}$ is a normalization constant. The AME2016 filter is obtained as

$$P_{AME2016}(\mathbf{X}) \propto \omega_{\mathrm{AME}}\ \mathrm{e}^{-\chi^2_{\mathrm{AME}}(\mathbf{X})/2}, \quad (18)$$

where, $\omega_{\mathrm{AME}} = 0$ or 1 depending on the meaningful reproduction or not, of the whole AME2016 mass table (Wang et al. 2017), respectively. The objective function for the AME2016 mass table is given by

$$\chi^2_{\mathrm{AME}}(\mathbf{X}) = \frac{1}{N}\sum_n \frac{\left((B/A)^{(n)}_{\mathrm{CLDM}}(\mathbf{X}) - (B/A)^{(n)}_{\mathrm{AME}}\right)^2}{\sigma^2_{\mathrm{BE}}}, \quad (19)$$

[3]The spin parameters have been fixed to reasonable values lying in the inferred range for the GW170817 event (Abbott et al. 2019).

[4]The 12 NMPs are: n_{sat}, $E_{(\mathrm{sat,sym})}$, L_{sym}, $K_{(\mathrm{sat,sym})}$, $Q_{(\mathrm{sat,sym})}$, and $Z_{(\mathrm{sat,sym})}$, plus the two effective masses m_q^* for neutrons and protons at saturation. The full function $m_q^*(n, \delta)$ in equation (1) is then uniquely fixed by following the parametrization in (Margueron et al. 2018).

with $N = 2408$ and the adopted error $\sigma_{\rm BE} = 0.04$ MeV. The probability for the χ-EFT pass-band type filter based on the constraints on SNM and PNM between $n = 0.02$ and $0.2\,{\rm fm}^{-3}$ is obtained from the theoretical calculation in Drischler et al. (2016) as,

$$P_{\chi\text{-EFT}}(\mathbf{X}) \propto \omega_{\chi\text{-EFT}}(\mathbf{X}), \tag{20}$$

where, $\omega_{\chi\text{-EFT}}(\mathbf{X}) = 0$ or 1, depending on SNM and PNM corresponding to $\mathbf{X}$ passing through the whole range or not. This theoretical band was obtained from the 90 per cent confidence interval, which we have increased by 5 per cent on the edges to interpret it as a 2σ band. The probability assigned to each model due to observed maximum mass $M_{\rm max}^{\rm obs} = 2.01 \pm 0.04\,{\rm M}_\odot$ (Antoniadis et al. 2013), following a cumulative probability distribution, is given by

$$P_{M_{\rm max}}(\mathbf{X}) = \frac{1}{0.04\sqrt{2\pi}} \int_0^{M_{\rm max}(\mathbf{X})/{\rm M}_\odot} {\rm e}^{-\frac{(x-2.01)^2}{2\times 0.04^2}}\,{\rm d}x. \tag{21}$$

The effect of the joint tidal deformability $\tilde{\Lambda}$ observed during the GW170817 event (Abbott et al. 2019) on the different metamodels and hybrid metamodels are obtained from a two-dimensional probability distribution $P_{GW170817}(\tilde{\Lambda}(q), q)$ as,

$$P_{GW170817}(\mathbf{X}) = \sum_i P_{GW170817}\left(\tilde{\Lambda}(q^{(i)}), q^{(i)}\right). \tag{22}$$

Here, we have assumed a constant $\mathcal{M}_{\rm c} = 1.186\,{\rm M}_\odot$ due to the small uncertainty in the observed chirp mass. For each model $\mathbf{X}$, we sampled $q \in [0.73, 1]$ and interpolated the probabilities from the two dimensional distribution $P_{GW170817}(\tilde{\Lambda}(q), q)$ to perform the sum in equation (22).

Once the informed prior probability for each model is obtained, the corresponding probability distribution for the observables is obtained by marginalizing over the range of parameters $\mathbf{X} \in [\mathbf{X}_{\rm min}, \mathbf{X}_{\rm max}]$ as,

$$P_{\rm prior}^{\rm informed}(Y) = \prod_{k=1}^{N} \int_{X_k^{\rm min}}^{X_k^{\rm max}} {\rm d}X_k\, P_{\rm prior}^{\rm informed}(\mathbf{X}) \delta\left(Y - Y(\mathbf{X})\right). \tag{23}$$

4.2 Confronting the models with simulated 'observations'

To identify the signature of a PT in the GW signal from a BNS coalescence, we examine the compatibility of the purely nucleonic metamodel and the hybrid metamodels subjected to a given event. As described in Section 4.2, we consider a hypothetical BNS coalescing event specified by $\{\mathcal{M}_{\rm c}^0, q_0, \tilde{\Lambda}_0\}$, where $\mathcal{M}_{\rm c}$ is the chirp mass, $q = m_2/m_1$ the mass ratio, and $\tilde{\Lambda}$ the tidal deformability. To determine $\tilde{\Lambda}_0(\mathcal{M}_{\rm c}^0, q_0)$ we use a specific EoS model from one of the hybrid metamodel families. Given the characteristics of the detector, the distance ($\mathcal{D}_{\rm L}$) and the sky location, we then calculate the interferometer response to this event via GWBENCH using the aforementioned EoS model. This gives us a posterior experimental distribution $p_{GW}^0(\mathcal{M}_c, q, \tilde{\Lambda})$, as well as the marginalized distributions $p_{GW}^0(\mathcal{M}_c)$, $p_{GW}^0(q)$, and $p_{GW}^0(\tilde{\Lambda})$, that of course will implicitly depend on the choice $\mathcal{M}_c^0, q_0$, together with the detector characteristics. Since the chirp mass is very well measured, we will always assume $p_{GW}^0(\mathcal{M}_c) = \delta(\mathcal{M}_c - \mathcal{M}_c^0)$.

Once an 'observation' is simulated with a model from the hybrid metamodel class, we want to confront the tidal polarizability measurement $p_{GW}^0(\tilde{\Lambda})$ with the nucleonic hypothesis. To make the comparison, in principle, we could calculate

$$p_{\rm meta}^{(0)}(\tilde{\Lambda}) \equiv p\left(\tilde{\Lambda} \mid meta, BI = \mathcal{M}_{\rm c}^0, q_0\right), \tag{24}$$

where *meta* denotes the nucleonic metamodel, and *BI* the background information. However, if we consider that $p_{GW}^0(\tilde{\Lambda})$ corresponds to a true measurement, $\mathcal{M}_c^0$ and q_0 are not known exactly, but only as a distribution $p_{GW}^0(\mathcal{M}_{\rm c}, q)$. Thus, the only quantity we can meaningfully compare to $p_{GW}^0(\tilde{\Lambda})$ is the distribution given by,

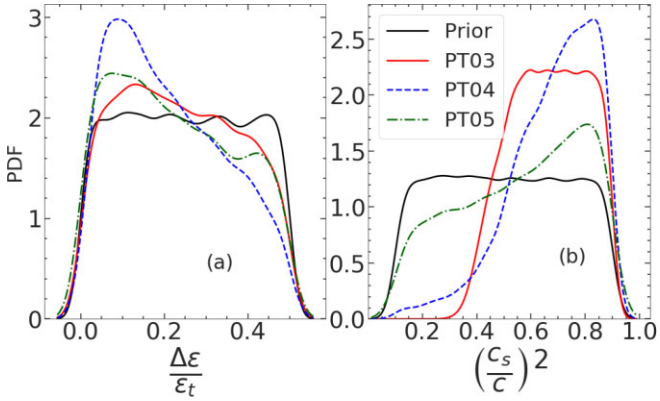

Figure 1. Informed prior distribution of the width of plateau $\Delta\varepsilon$ in units of energy density at transition ε_t and squared sound speed c_s^2 in units of speed of light c with PTs at 0.3, 0.4, and $0.5\,{\rm fm}^{-3}$ for hybrid metamodels PT03, PT04, and PT05, respectively (see text for details).

$$p_{\rm meta}^{(1)}(\tilde{\Lambda}) \equiv p\left(\tilde{\Lambda} \mid meta, BI = \mathcal{M}_{\rm c}^0, p_{GW}^0(q)\right). \tag{25}$$

Imposing to the nucleonic metamodel a q distribution identical to the one hypothetically extracted from the 'observation' clearly gives a distribution more spread than $p_{\rm meta}^{(0)}(\tilde{\Lambda})$, which is the only one that we will be able to compare to the observation. A similar probability distribution corresponding to the hybrid metamodel is expressed as

$$p_{\rm PT}^{(1)}(\tilde{\Lambda}) \equiv p\left(\tilde{\Lambda} \mid PT, BI = \mathcal{M}_{\rm c}^0, p_{GW}^0(q)\right), \tag{26}$$

where *PT* signifies hybrid metamodels containing a first-order hadron-quark PT.

In the end, to distinguish the compatibility of observation with the nucleonic metamodel and the hybrid metamodels, one can resort to evidence in terms of Bayes factors. Given an event, the Bayes factor can be defined as a function of $\tilde{\Lambda}$ as

$$B_{\rm PT,meta}(\tilde{\Lambda}) = \frac{p_{\rm PT}^{(1)}(\tilde{\Lambda})}{p_{\rm meta}^{(1)}(\tilde{\Lambda})}, \tag{27}$$

$$B_{\rm meta,PT}(\tilde{\Lambda}) = \frac{1}{B_{\rm PT,meta}(\tilde{\Lambda})}. \tag{28}$$

The average Bayes factors associated to the simulated observation $p_{GW}^0(\tilde{\Lambda})$ is specified as

$$\log\left(\langle B\rangle_{\rm PT,meta}^{\mathcal{M}_{\rm c}^0, q_0}\right) = \int {\rm d}\tilde{\Lambda}\; p_{GW}^0(\tilde{\Lambda}) \log\left[\frac{p_{\rm PT}^{(1)}(\tilde{\Lambda})}{p_{\rm meta}^{(1)}(\tilde{\Lambda})}\right], \tag{29}$$

$$\log\left(\langle B\rangle_{\rm meta,PT}^{\mathcal{M}_{\rm c}^0, q_0}\right) = \int {\rm d}\tilde{\Lambda}\; p_{GW}^0(\tilde{\Lambda}) \log\left[\frac{p_{\rm meta}^{(1)}(\tilde{\Lambda})}{p_{\rm PT}^{(1)}(\tilde{\Lambda})}\right]. \tag{30}$$

5 RESULTS

5.1 Hybrid metamodels

To set the stage for confronting simulated observations with families of EoS with or without a PT to quark matter, we need to obtain an informed prior as described by equations (17) and (23). Distributions of these informed priors for different nuclear matter parameters of the nucleonic metamodelling can be found in Dinh Thi et al. (2021a) and Mondal & Gulminelli (2023) as posteriors. In Fig. 1, we display the distributions of the sound speed parameter c_s^2 in panel (a) and

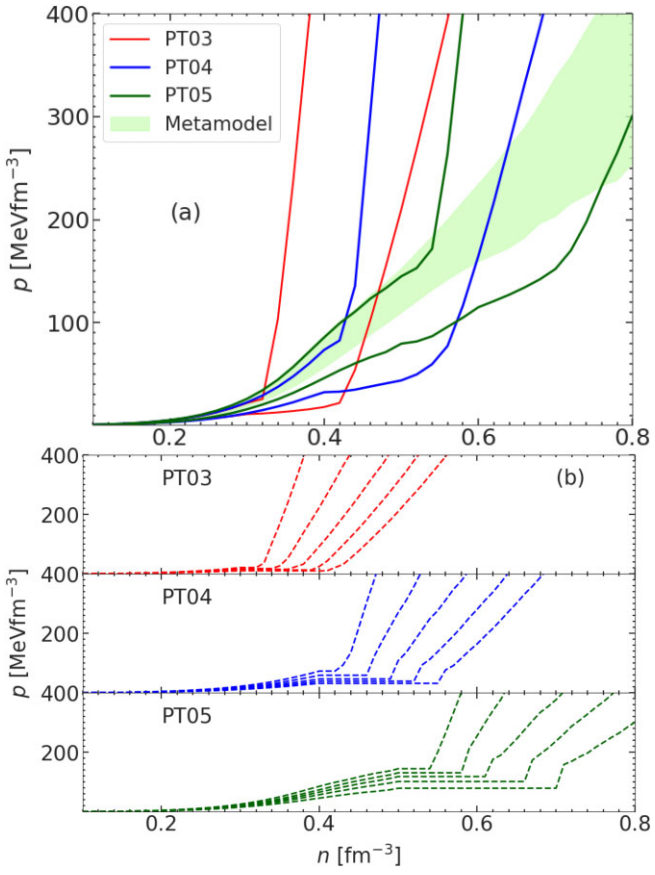

Figure 2. (a) Pressure at β-equilibrium as a function of number density n at the 1σ confidence interval obtained for nucleonic metamodel and hybrid metamodels PT03, PT04, and PT05; (b) Injection models with first-order PTs based on the intervals given in panel (a) obtained for simulated 'observations' using GWBENCH (see text for more details).

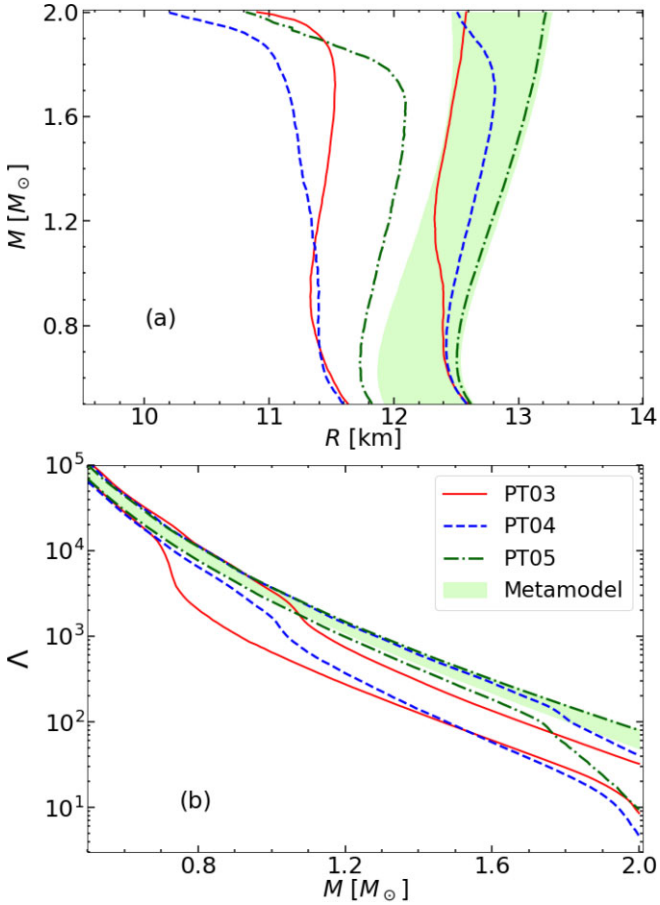

Figure 3. M–R and Λ-M relations at 1σ confidence interval obtained for nucleonic metamodel and hybrid metamodels PT03, PT04, and PT05.

width of the plateau $\Delta\varepsilon$ in panel (b) for the new class of hybrid metamodels PT03, PT04, and PT05, as described in Section 2.1.2 and 4. To highlight the impact of the astrophysical constraints like the observed $M_{\rm max}$ or $\tilde{\Lambda}$ from GW170817 on the hybrid metamodels, we display the prior distributions of $\Delta\varepsilon$ and c_s^2 in Fig. 1, too. For PT03, models with small values of c_s^2 ($< 0.4c^2$) get suppressed significantly, but the rest still remain uniformly distributed. The hybrid metamodel PT04 clearly prefers to have larger c_s^2, which somewhat evens out for PT05. The distributions of $\Delta\varepsilon$ for different hybrid metamodels obtain crests at smaller values (*i.e.* no first-order PT) compared to the uninformed flat prior.

In Fig. 2(a) we display the EoS of the nucleonic metamodel along with hybrid metamodels PT03, PT04, and PT05 in a 1σ confidence interval. We remind that these EoS posteriors are consistent with various observational constraints as described in Section 4.1. One can observe that with increasing transition density $n_{\rm t}$ from nucleonic to quark matter, the overall region explored in the p–n plane increases. An early PT requires a very stiff behaviour of the quark phase, such as to meet the $2\,{\rm M}_\odot$ constraint. On the other hand, relatively softer behaviours, corresponding to lower values of the c_s^2 parameter, are allowed if the quark phase emerges at higher densities. This is consistent with the distribution of c_s^2 displayed in Fig. 1(b).

In order to simulate hypothetical observations within the Fisher formalism, one needs specific injection EoS models. We chose different injection models for PT03, PT04, and PT05 guided by the 1σ boundaries displayed in Fig. 2(a). The representative injection EoS are displayed in Fig. 2(b) for PT03, PT04, and PT05 hybrid metamodels, respectively. Except for the plateau region, each individual injection model follows the 16, 33, 50, 67, and 84 per cent quantiles of the corresponding posteriors from the bottom to the top (or right to left), respectively. We follow the nomenclature for the injection models obtained at the 16 and 84 per cent quantiles as '1σ-lower' and '1σ-upper' models (c.f. Figs 4–7) of the corresponding hybrid metamodel classes i.e. PT03, PT04, and PT05, respectively. The three versions (PT03, PT04, and PT05) of the 1σ-lower models share by construction the same low-density behaviour, and the same is true for the three versions of the 1σ-upper models. It is interesting to observe that the posterior distribution of the nuclear parameters up to order two (i.e. $E_{\rm sat}$, $E_{\rm sym}$, $L_{\rm sym}$, $K_{\rm sat}$, and $K_{\rm sym}$), conditioned by the $\tilde{\Lambda}$ observation, turn out to be the same in all the different classes of models, independent on the occurrence of the PT and on the density at which it occurs. This means that whatever the density of occurrence of the PT (above 2 $n_{\rm sat}$), meaningful values for those parameters can be extracted from a meta-model analysis of the GW signals.

In Fig. 3 we plot the two-dimensional informed prior distribution for M–R (panel a) and Λ-M (panel b) relations of NSs using nucleonic and different hybrid metamodels. Introducing a first-order hadron-quark PT (c.f. Fig. 2a) in the hybrid metamodels and the further requirements from various astrophysical constraints categorically soften the EoS. However, this does not systematically shift the hybrid metamodels to explore smaller R or Λ at a given M, with incremental

Table 1. Different GWBENCh injection parameters which were varied are listed. For all of them, $\chi_1 = 0.01$, $\chi_2 = 0.005$, and $\iota = 45^\circ$ were kept fixed. $\tilde{\Lambda}$ and $\delta\tilde{\Lambda}$ were fixed by the underlying injection models depicted in Fig. 2(b).

Parameter	Range	Step-size
$\mathcal{M}_c^0$ ($M_\odot$)	1.1–1.46	0.045
$q_0 = \frac{m_2}{m_1}$	0.79–0.99	0.05
$\mathcal{D}_L$ (Mpc)	22, 120, 221, 326, 433, 544, 657, 772, 891, 1012	

n_t i.e. from 0.3 to 0.5 fm^{-3} due to the behaviour of the nucleonic model in between the different transition densities. Beyond 1.2 $M_\odot$, PT03 and the nucleonic metamodel explore almost complementary regions in the M–R and Λ-M planes at the $1-\sigma$ level. The overlap regions increase significantly between PT04 and nucleonic metamodel for both M–R and Λ-M. At larger masses (>1.5 $M_\odot$) PT04 also explores smaller R and Λ compared to the other families of hybrid metamodels considered in this work. PT05 almost engulfs the nucleonic metamodel, additionally exploring smaller values of R and Λ at larger masses (>1.7 $M_\odot$). Essentially these differences in Λ displayed in Fig. 3 are manifested in the joint tidal deformability $\tilde{\Lambda}$, which is explored in detail in the next section.

5.2 Simulated observations

As an exploratory study, we start by considering single events, choosing at each time specific values of chirp mass $\mathcal{M}_c^0$, mass ratio q_0, and luminosity distance $\mathcal{D}_L$ keeping the remaining parameters defining a BNS coalescence, *viz.* spin $\vec{\chi}$ of the constituents, inclination ι etc. fixed. Altogether, we considered nine values of $\mathcal{M}_c^0$, five values of q_0 situated at 10 different $\mathcal{D}_L$ as outlined in Table. 1. The response of the Fisher matrix formalism for a chosen EoS was tested for these 450 assumed events with equal probability. Five different hybrid EoSs from each of the PT03, PT04, and PT05 families were used for this purpose, which are displayed explicitly in Fig. 2(b). Note that we use the notation $\mathcal{M}_c$ and q instead of $\mathcal{M}_c^0$ and q_0, from here onward, respectively. This is just for simplicity. We want to emphasize here that assumptions about the chosen events, and how they are distributed in the sky can affect the quantitative outcomes we are going to demonstrate in this section. However, the methodology proposed here can be used to incorporate models of NS mass distributions (see e.g. Özel & Freire 2016). We leave it as a future study.

Before diving into the calculation of Bayes factors as demonstrated in equations (29)–(30), let us first analyse the premises chosen in the different astrophysical parameters and EoS modelling for the present endeavour. To this aim, we compare systematically the PDFs of $\tilde{\Lambda}$ of BNS merging events that enter in equations (29)–(30), i.e. $p^0_{GW}(\tilde{\Lambda})$, $p^{(1)}_{PT}(\tilde{\Lambda})$, and $p^{(1)}_{meta}(\tilde{\Lambda})$ calculated from GWBENCH, hybrid and nucleonic metamodels, respectively, changing one variable at a time, keeping the rest fixed. In Fig. 4, we plot the PDFs of $\tilde{\Lambda}$ calculated from nucleonic metamodel (blue), hybrid metamodel PT03 (green) and GWBENCH (red) for two extreme mass ratios $q = 0.79$ (solid lines) and $q = 0.99$ (dashed lines) considered in the present calculation. In both cases, $\mathcal{M}_c = 1.19\,M_\odot$ and $\mathcal{D}_L = 22$ Mpc were kept fixed and the same injection model PT03-1σ-lower was used in GWBENCH. The differences due to the variation in q are almost negligible. In the case of a very close detection shown in Fig. 4, the theoretical uncertainties clearly prime over the observational ones. In spite of those large uncertainties, the two theoretical distributions only marginally overlap. The Bayes factors calculated for $q = 0.79$ and 0.99 as depicted in Fig. 4 using equation (29) turned out to be $\log\left(\langle B\rangle^{1.19\ M_\odot,0.79}_{\rm PT03,meta}\right) = 2.15$ and $\log\left(\langle B\rangle^{1.19\ M_\odot,0.99}_{\rm PT03,meta}\right) = 1.56$, respectively. We have observed that the quantitative values of the Bayes factors demonstrated here can further increase if a larger $\mathcal{M}_c$ is chosen.

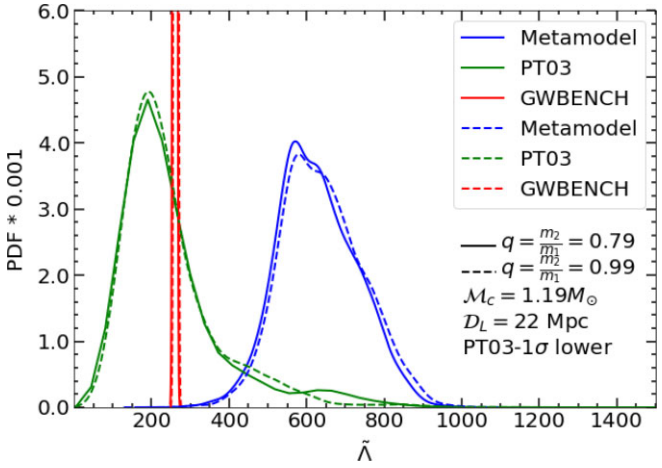

Figure 4. Probability distribution functions (PDFs) of joint tidal deformability $\tilde{\Lambda}$ in nuclonic metamodel, hybrid metamodel PT03 and GWBENCH for mass ratio $q = 0.79$ (solid) and $q = 0.99$ (dashed) obtained using PT03-1σ-lower injection model, $\mathcal{M}_c = 1.19\,M_\odot$ and $\mathcal{D}_L = 22$ Mpc.

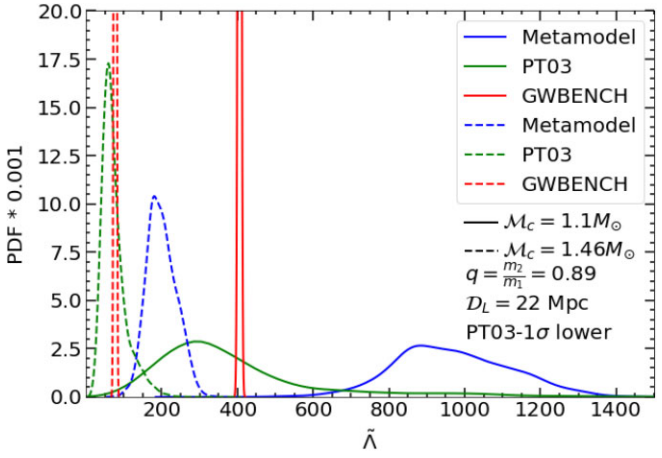

Figure 5. The same as Fig. 4 but for $\mathcal{M}_c = 1.1\,M_\odot$ (solid) and $\mathcal{M}_c = 1.46\,M_\odot$ (dashed) using PT03-1σ-lower injection model, $q = 0.89$ and $\mathcal{D}_L = 22$ Mpc.

This is exactly what is analysed in Fig. 5, where we show the PDFs of $\tilde{\Lambda}$ calculated from the nucleonic metamodel (blue) and one of its hybrid counterparts PT03 (green) along with GWBENCH (red) for two extreme cases of chirp masses $\mathcal{M}_c = 1.1\,M_\odot$ (solid lines) and $1.46\,M_\odot$ (dashed lines) considered in the present calculation. The same injection model PT03-1σ-lower was used in this study as in Fig. 4. The mass ratio q and luminosity distance $\mathcal{D}_L$ was kept fixed at 0.89 and 22 Mpc, respectively. Clearly, the difference in $\mathcal{M}_c$ results in a change in the position of the peaks of the PDFs as well as their widths. The particular scenario depicted in Fig. 5 for $\mathcal{M}_c = 1.1\,M_\odot$ and $1.46\ M_\odot$ results in a big difference in the Bayes factors, $\log\left(\langle B\rangle^{1.1\ M_\odot,0.89}_{\rm PT03,meta}\right) = 1.54$ and 3.22, respectively. In general, the effect of $\mathcal{M}_c$ is found to be much stronger in the Bayes factor compared to the mass ratio q, if the rest of the variables are kept

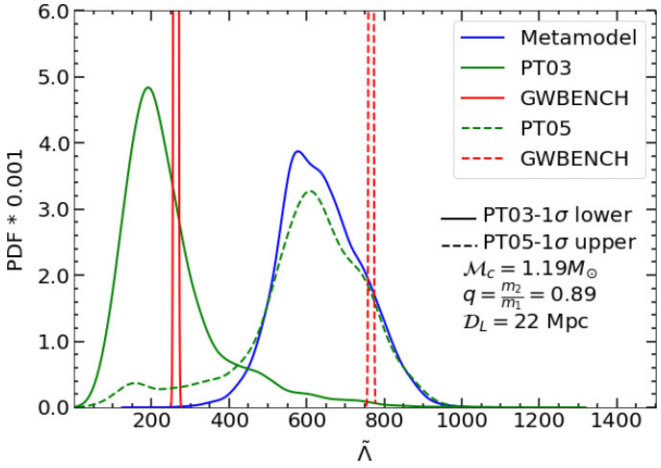

Figure 6. The same as Fig. 4 but for injection models PT03-1σ-lower (solid) and PT05-1σ-upper (dashed) using $\mathcal{M}_c = 1.19\ M_\odot$, $q = 0.89$, and $\mathcal{D}_L = 22$ Mpc.

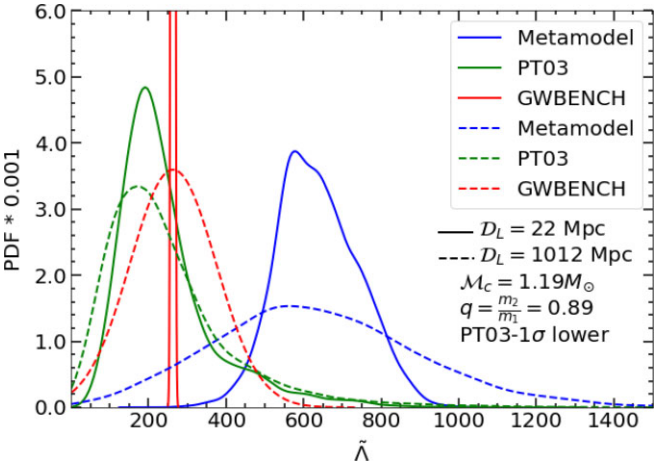

Figure 7. The same as Fig. 4 but for $\mathcal{D}_L = 22$ Mpc (solid) and 1012 Mpc (dashed) using PT03-1σ-lower injection model, $\mathcal{M}_c = 1.19\ M_\odot$ and $q = 0.89$.

fixed. Identification of the first-order PT will thus be more probable from the future observations for events with larger $\mathcal{M}_c$'s.

We lay our focus on the impact of injection models on the PDFs of $\tilde{\Lambda}$ in Fig. 6. Like the analysis done in Figs 4 and 5, there is no exact guide to choose two extreme injection models from the ones outlined in Fig. 2(b). Keeping an eye on Fig. 2(a), we choose PT03-1σ-lower and PT05-1σ-upper with the idea that they have the least and maximum overlap with the nucleonic metamodel, respectively. PDFs of $\tilde{\Lambda}$ obtained using PT03-1σ-lower (solid lines) and PT05-1σ-upper (dashed lines) are displayed in Fig. 6 for the nucleonic metamodel (blue), hybrid metamodels (green), and GWBENCH (red). One should note that, depending on the injection models we display the corresponding hybrid metamodels PT03 and PT05, respectively. Since the underlying astrophysical event is the same with $\mathcal{M}_c = 1.19\,M_\odot$, $q = 0.89$, and $\mathcal{D}_L = 22$ Mpc, the PDF of $\tilde{\Lambda}$ obtained with nucleonic metamodel appears as a common one for both the injection models. The Bayes factors for the cases considered in Fig. 6 turn out to be $\log\left(\langle B\rangle^{1.19\,M_\odot,0.89}_{\rm PT03,meta}\right) = 1.79$ and 0.02 for PT03-1σ-lower and PT05-1σ-upper, respectively. This gives already an indication that identifying an early hadron-quark first-order PT will be more probable than a later one from future GW signals.

Depending on how far one BNS merger event takes place, the SNR recorded in GW interferometers can vary a lot. We have analysed, to this aim, an event with $\mathcal{M}_c = 1.19\,M_\odot$ and $q = 0.89$ simulated using PT03-1σ-lower injection model at luminosity distances $\mathcal{D}_L = 22$ Mpc (solid lines) and 1012 Mpc (dashed lines) in Fig. 7. The PDFs of $\tilde{\Lambda}$ corresponding to the nucleonic metamodel, hybrid metamodel PT03, and GWBENCH are displayed in blue, green, and red, respectively. The broadening of the PDFs from the case with $\mathcal{D}_L = 22$ Mpc to the case with $\mathcal{D}_L = 1012$ Mpc is clearly visible, which eventually affects the calculation of Bayes factors using equation (29). For $\mathcal{D}_L = 22$ Mpc, the Bayes factor is $\log\left(\langle B\rangle^{1.19\,M_\odot,0.89}_{\rm PT03,meta}\right) = 1.79$ (same as the one obtained from the solid lines in Fig. 6); for $\mathcal{D}_L = 1012$ Mpc the Bayes factor becomes $\log\left(\langle B\rangle^{1.19\,M_\odot,0.89}_{\rm PT03,meta}\right) = 0.76$. Even though in this particular case depicted in Fig. 7, there is a clear hint of hybrid metamodel to be preferred over the nucleonic one, the evidence is not significant enough, even if we suppose an early PT. To have the global picture of the PT detectability, we plot the Bayes factors at different luminosity distances $\mathcal{D}_L$ comparing PT03, PT04, and PT05 against the nucleonic

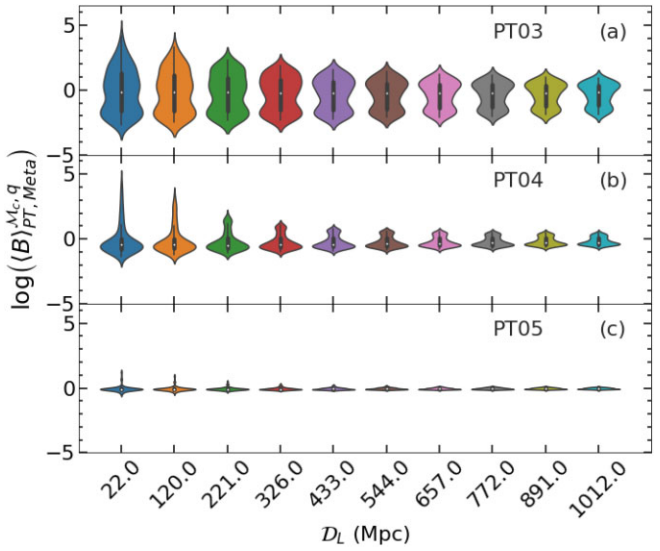

Figure 8. Average Bayes factor as a function of luminosity distance $\mathcal{D}_L$ for different injection models, averaged over the respective class of hybrid metamodels using equation (29). The distributions come from the variation in q and $\mathcal{M}_c$ considered in the present calculation (see Table 1).

metamodel in panels (a), (b), and (c) of Fig. 8, respectively. In each panel, at a given $\mathcal{D}_L$, the variation in $\log\left(\langle B\rangle^{\mathcal{M}_c,q}_{\rm PT,meta}\right)$ comes from the variation in $\mathcal{M}_c$, q, and injections models. Since we are interested in identifying the notion of a PT, high values of $\log\left(\langle B\rangle^{\mathcal{M}_c,q}_{\rm PT,meta}\right) \geq 1$–2 is our primary concern (Kass & Raftery 1995). From Fig. 8(c) it is evident that the existence of a first-order transition at around 0.5 fm^{-3} ($\sim 3n_{\rm sat}$) can't be identified from a single GW signal with third-generation interferometers. In Fig. 8(a) the other extreme case considered in the present calculation, i.e. a PT at 0.3 fm^{-3} ($\sim 2n_{\rm sat}$) se ems to be a viable situation that can be identified particularly with high confidence at distances less than 300 Mpc. The highest positive values of $\log\left(\langle B\rangle^{\mathcal{M}_c,q}_{\rm PT,meta}\right)$ at almost all distances are associated with larger $\mathcal{M}_c$'s obtained using injection models with lower quantiles (see Fig. 2(b) and the corresponding discussion). It seems from Fig. 8(b) that only for a small percentage of events at low luminosity distances ($\mathcal{D}_L \lesssim 100$ Mpc) a PT can be identified if nature prefers

to have it at $\sim 0.4\,\mathrm{fm}^{-3}$. Particularly, at $\mathcal{D}_\mathrm{L} = 22\,\mathrm{Mpc}$ the high $\log\left(\langle B\rangle^{\mathcal{M}_\mathrm{c},q}_{\mathrm{PT,meta}}\right)$ values correspond to $\mathcal{M}_\mathrm{c} > 1.4\,\mathrm{M}_\odot$ obtained with PT04-1σ-lower injection model. We expect that the detectability of a first-order PT reported in this study will be largely improved by considering multiple detections, as expected by the future ET. To this aim, we plan to study the evolution of the Bayes factors as a function of the number of detections, by including realistic population distributions.

6 SUMMARY AND DISCUSSION

In summary, we have presented an updated metamodelling technique for the EoS in NS matter including potential first-order hadron-quark PT. The hadronic core is assumed to have only nucleons and leptons up to a specified density. The EoS for the nucleonic core is obtained by an optimized expansion in number density truncated at fourth order following (Margueron et al. 2018). The crust EoS and composition are subsequently extracted with a unified approach in the spherical Wigner–Seitz approximation. The extension of the EoS modelling in the quark core is done with the constant sound speed model, without dwelling on the microscopic composition.

Three classes of hybrid (nucleon + quark) metamodels PT03, PT04, and PT05 named after the density corresponding to the hadron–quark PT, i.e. 0.3, 0.4, and $0.5\,\mathrm{fm}^{-3}$, respectively, were generated. These hybrid metamodels were already made compliant with different nuclear physics and astrophysics constraints within the Bayesian paradigm. Using these hybrid and nucleonic posteriors, we proposed a framework based on Bayes factors to discriminate a possible sign of PT from future GW signals generated by BNS mergers. To simulate future observational signals, we used the Fisher matrix formalism employing the publicly available tool GWBENCH (Borhanian 2021) that simulates the GW signal using the TaylorF2 + tidal waveform templates and includes the detector features of the projected third-generation ground-based interferometers. We considered a single detection, and compared different chosen cases corresponding to different masses of NSs, located at different distances, and using injection models which include first-order PT. In particular, these hybrid injection models were constructed out of PT03, PT04, and PT05 1σ posteriors, which are already informed by different physical constraints. We have critically assessed the impact of diversified variables in the discrimination of a PT signature through the Bayes factors.

We have found that the mass ratio of the constituents of a BNS merger does not play a significant role in the magnitude of the Bayes factors. Overall, higher chirp mass, smaller luminosity distances and early PT with strong first-order effect can facilitate a possible identification of PT from future GW signals. Further, we have found that if nature prefers to have a PT at higher densities ($\gtrsim 3n_\mathrm{sat}$), it is most likely to be masked, since it would be possible to explain that with an EoS model without PT. This is in qualitative agreement with the conclusions of references (Tan et al. 2022; Mroczek et al. 2023). An interesting prospect of the present study could also be to quantify how distinguishable the different PT models are from each other for a given event. The detailed work is in progress. In a preliminary observation, we found that the distinguishability of PT05 and PT03 is similar to the one of PT03 with respect to the case of no transition. This is because the $\tilde{\Lambda}$ response of the PT05 model is very close to one of the purely nucleonic models except for very high mass stars with low tidal deformabilities difficult to measure precisely. We expect that PT03 and PT04 will be hardly distinguishable even at very small distances, due to the large overlap between the regions for $\Lambda(M)$ predicted by the two models at least with the relatively important $\tilde{\Lambda}$ uncertainty associated with a single observation. This study is directed mostly towards structuring a framework to look for the signatures of PT in future GW signals generated by BNS mergers. A further study incorporating realistic population models is needed to estimate the effect of multiple detections. It is also going to be important to incorporate microscopic modelling in the quark phase to extract further physical information regarding composition at high densities. We leave these ventures for future studies.

ACKNOWLEDGEMENTS

We would like to thank Anthea Fantina for enlightening discussions as well as a careful reading of the manuscript, and Ssohrab Borhanian for fruitful exchanges and support on gwbench. This work has been partially supported by the IN2P3 Master Project NewMAC and the ANR project GWsNS, contract ANR-22-CE31-0001-01. The authors gratefully acknowledge the Italian Instituto Nazionale de Fisica Nucleare (INFN), the French Centre National de la Recherche Scientifique (CNRS), and the Netherlands Organization for Scientific Research for the construction and operation of the Virgo detector and the creation and support of the EGO consortium.

DATA AVAILABILITY

No new data were generated in support of this research. The numerical results and the code underlying this article will be shared upon reasonable request to the authors.

REFERENCES

Abbott B. P., et al., 2017, Phys. Rev. Lett., 119, 161101
Abbott B. P., et al., 2019, Phys. Rev. X, 9, 011001
Alford M. G., 2001, Ann. Rev. Nucl. Part. Sci., 51, 131
Alford M. G., Sedrakian A., 2017, Phys. Rev. Lett., 119, 161104
Alvarez-Castillo D. E., Blaschke D. B., Grunfeld A. G., Pagura V. P., 2019, Phys. Rev. D, 99, 063010
Antoniadis J., et al., 2013, Science, 340, 6131
Bauswein A., Bastian N.-U. F., Blaschke D. B., Chatziioannou K., Clark J. A., Fischer T., Oertel M., 2019, Phys. Rev. Lett., 122, 061102
Blacker S., Bastian N.-U. F., Bauswein A., Blaschke D. B., Fischer T., Oertel M., Soultanis T., Typel S., 2020, Phys. Rev. D, 102, 123023
Borhanian S., 2021, Class. Quantum Gravity, 38, 175014
Branchesi M. et al., 2023, preprint (arXiv:2303.15923)
Buballa M. et al., 2014, J. Phys. G, 41, 123001
Burgio F. G., Fantina A. F., 2018, Astrophys. Space Sci. Libr., 457, 255
Carreau T., Gulminelli F., Margueron J., 2019, Eur. Phys. J. A, 55, 188
Chamel N., Haensel P., 2008, Living Rev. Rel., 11, 10
Chatziioannou K., Han S., 2020, Phys. Rev. D, 101, 044019
Chatziioannou K., Haster C.-J., Zimmerman A., 2018, Phys. Rev. D, 97, 104036
Chen H., Wei J. B., Baldo M., Burgio G. F., Schulze H. J., 2015, Phys. Rev. D, 91, 105002
Chen H.-Y., Chesler P. M., Loeb A., 2020, Astrophys. J. Lett., 893, L4
Contrera G. A., Blaschke D., Carlomagno J. P., Grunfeld A. G., Liebing S., 2022, Phys. Rev. C, 105,045808
Coupechoux J. F., Chierici R., Hansen H., Margueron J., Somasundaram R., Sordini V., 2023, Phys. Rev. D, 107, 124006
Cromartie H. T., et al., 2019, Nat. Astron., p. 439
Cutler C., Flanagan E. E., 1994, Phys. Rev. D, 49, 2658
Damour T., Nagar A., 2009, Phys. Rev. D, 80, 084035
Demorest P., Pennucci T., Ransom S., Roberts M., Hessels J., 2010, Nature., 467, 1081
Dinh Thi H., Mondal C., Gulminelli F., 2021a, Universe, 7, 373
Dinh Thi H., Fantina A. F., Gulminelli F., 2021b, Eur. Phys. J. A, 57, 296

Dinh Thi H., Carreau T., Fantina A. F., Gulminelli F., 2021c, Astron. Astrophys., 654, A114
Drischler C., Hebeler K., Schwenk A., 2016, Phys. Rev. C, 93, 054314
Essick R., Tews I., Landry P., Reddy S., Holz D. E., 2020, Phys. Rev. C, 102, 055803
Evans M. et al., 2021, preprint (arXiv:2109.09882)
Fonseca E. et al., 2016, ApJ, 832, 167
Glendenning N. K., Weber F., Moszkowski S. A., 1992, Phys. Rev. C, 45, 844
Haensel P., Potekhin A., Yakovlev D., 2007, Astrophysics and Space Science Library, Vol. 326, Neutron Stars 1: Equation of State and Structure. Springer New York,
Han S., Steiner A. W., 2019, Phys. Rev. D, 99, 083014
Hinderer T., 2008, ApJ, 677, 1216
Hinderer T., 2009, ApJ, 697, 964
Jokela N., Järvinen M., Nijs G., Remes J., 2021, Phys. Rev. D, 103, 086004
Kass R. E., Raftery A. E., 1995, J. Am. Stat. Assoc., 90, 773
Kurkela A., Romatschke P., Vuorinen A., 2010, Phys. Rev. D, 81, 105021
Landry P., Chakravarti K., 2022, preprint (arXiv:2212.09733)
Landry P., Essick R., Chatziioannou K., 2020, Phys. Rev. D, 101, 123007
Lattimer J. M., 2019, Ann. Phys., 411, 167963
Maggiore M. et al., 2020, J. Cosmol. Astropart. Phys., 2020, 050
Margueron J., Hoffmann Casali R., Gulminelli F., 2018, Phys. Rev. C, 97, 025805
Maruyama T., Tatsumi T., Voskresensky D. N., Tanigawa T., Chiba S., 2005, Phys. Rev. C, 72, 015802
Miller M. C., et al., 2019, ApJ, 887, L24
Miller M. C., et al., 2021, ApJ, 918, L28
Mondal C., Gulminelli F., 2023, Phys. Rev. C, 107, 015801
Most E. R., Papenfort L. J., Dexheimer V., Hanauske M., Schramm S., Stöcker H., Rezzolla L., 2019, Phys. Rev. Lett., 122, 061101
Mroczek D., Miller M. C., Noronha-Hostler J., Yunes N., 2023, preprint (arXiv:2302.07978)
Newton W. G., Gearheart M., Li B.-A., 2013, A&AS, 204, 9
Oertel M., Hempel M., Klähn T., Typel S., 2017, Rev. Mod. Phys., 89, 015007
Otto K., Oertel M., Schaefer B.-J., 2020, Phys. Rev. D, 101, 103021
Özel F., Freire P., 2016, Ann. Rev. Astron. Astrophys., 54, 401
Pang P. T. H., Dietrich T., Tews I., Van Den Broeck C., 2020, Phys. Rev. Res., 2, 033514
Pereira J. P., Bejger M., Andersson N., Gittins F., 2020, ApJ, 895, 28
Poisson E., Will C. M., 1995, Phys. Rev. D, 52, 848
Postnikov S., Prakash M., Lattimer J. M., 2010, Phys. Rev. D, 82, 024016
Punturo M. et al., 2010, Class. Quantum Gravity, 27, 194002
Raduta A. R., 2022, Eur. Phys. J. A, 58, 115
Raithel C. A., Most E. R., 2023, Phys. Rev. Lett., 130, 201403
Ravenhall D. G., Pethick C. J., Lattimer J. M., 1983, Nucl. Phys. A, 407, 571
Reitze D. et al., 2019, Bull. Am. Astron. Soc., 51, 035
Riley T. E. et al., 2019, ApJ, 887, L21
Riley T. E. et al., 2021, ApJ, 918, L27
Shahrbaf M., Antić S., Ayriyan A., Blaschke D., Grunfeld A. G., 2023, Phys. Rev. D, 107, 054011
Sieniawska M., Turczanski W., Bejger M., Zdunik J. L., 2019, A&A, 622, A174
Tan H., Dexheimer V., Noronha-Hostler J., Yunes N., 2022, Phys. Rev. Lett., 128, 161101
Torres-Rivas A., Chatziioannou K., Bauswein A., Clark J. A., 2019, Phys. Rev. D, 99, 044014
Vallisneri M., 2008, Phys. Rev. D, 77, 042001
Wade L., Creighton J. D. E., Ochsner E., Lackey B. D., Farr B. F., Littenberg T. B., Raymond V., 2014, Phys. Rev. D, 89, 103012
Wang M., Audi G., Kondev F. G., Huang W., Naimi S., Xu X., 2017, Chin. Phys. C, 41, 030003
Weih L. R., Hanauske M., Rezzolla L., 2020, Phys. Rev. Lett., 124, 171103
Xu S.-S., Yan Y., Cui Z.-F., Zong H.-S., 2015, Int. J. Mod. Phys. A, 30, 1550217
Zacchi A., Hanauske M., Schaffner-Bielich J., 2016, Phys. Rev. D, 93, 065011
Zdunik J. L., Haensel P., 2013, A&A, 551, A61
Zhang N.-B., Li B.-A., 2023, preprint (arXiv:2304.07381)

This paper has been typeset from a TEX/LATEX file prepared by the author.